ELSEVIER

Cassini RPWS observations of dust in Saturn's E Ring

W.S. Kurth*, T.F. Averkamp, D.A. Gurnett, Z. Wang

Department of Physics and Astronomy, The University of Iowa, Iowa City, IA 52242, USA

Abstract

The Cassini radio and plasma wave science (RPWS) instrument is sensitive to few-micron dust grains impacting on the spacecraft at relative speeds of order 10 km/s. Through the first year or so of operations in orbit at Saturn, the RPWS has made a number of both inclined and equatorial crossings of the E ring, particularly near the orbit of Enceladus. Assuming water ice grains, the typical size particle detected by the RPWS has a radius of a few microns. Peak impact rates of about $50\,s^{-1}$ are found near the orbit of Enceladus corresponding to densities of order $5 \times 10^{-4}\,m^{-3}$. The variation of dust fluxes as a function of height above or below the equator is well described by a Gaussian distribution with a scale height of about 2800 km although there is usually some non-Gaussian variation near the peak fluxes suggesting some structure in the core of the ring. Offsets of the peak number densities are typically of the order of a few hundred km from the geometric equator. A near-equatorial radial profile through the orbit of Enceladus shows a sharply peaked distribution at the orbit of the moon. A size distribution averaged over several passes through the orbit of Enceladus is determined which varies as $m^{-2.80}$. The peak in dust number density at the orbit of Enceladus is consistent with previous optical measurements and strongly supports the suggestion that Enceladus is a primary source for E ring particles.
© 2006 Elsevier Ltd. All rights reserved.

Keywords: Saturn; E ring; Dust; Cassini

1. Introduction

The E ring at Saturn was first detected by Earth-based optical observations during Earth's crossing through Saturn's equator in 1966 (Feibelman, 1984). The first in situ measurements of E ring particles were by Humes et al. (1980), Tsintikidis et al. (1995) and Meyer-Vernet et al. (1996). The E ring has a pronounced peak in brightness at the orbit of Enceladus and, therefore, it has been assumed that Enceladus is the primary source of the E ring (Haff et al., 1983). Further, Morfill et al. (1993) have suggested that the E ring may be a major source of neutral gas and plasma in Saturn's magnetosphere, although Johnson et al. (1989) suggest the latter may come directly from the icy moons. Showalter et al. (1991) provide a thorough summary of optical observations of the E ring and conclude that the E ring is composed of a narrow size range of water ice grains with radii very close to 1 μm. This

size was reported by Meyer-Vernet et al. (1996) using Voyager 1 planetary radio astronomy measurements. The Cassini orbital tour now provides for concerted in situ studies of the E ring by Cassini's cosmic dust analyzer (CDA) and the radio and plasma wave science (RPWS) investigations. This paper presents the first observations of E ring dust by the RPWS.

The Voyager 2 flyby of Saturn just outside the G ring in 1980 demonstrated that radio astronomy and plasma wave instruments are sensitive to micron-sized dust impacts on a spacecraft. Gurnett et al. (1983) showed that the impacts resulted in a voltage pulse at the input to the electric antenna preamplifiers and that these impulses could be counted to give a very accurate measure of the rate of impacts. They also estimated the size of the impacts based on the estimated charge yield of the impacts and other considerations. Aubier et al. (1983) reported that the ensemble effect of multiple dust impacts is a spectrum, which varies as f^{-4} at high frequencies and that the break point in this spectrum is related to the mass of the impacting particles. Both instruments provided evidence of

*Corresponding author. Tel.: +1 319 335 1926; fax: +1 319 335 1753.
E-mail address: william-kurth@uiowa.edu (W.S. Kurth).

micron-sized dust in the equatorial planes of Uranus and Neptune, as well (Gurnett et al., 1987, 1991; Meyer-Vernet et al., 1986; Pedersen et al., 1991).

The RPWS instrument on Cassini (Gurnett et al., 2004) is also sensitive to micron-sized dust particles impacting the spacecraft. There is sufficient kinetic energy in these collisions with relative velocities of order 10 km/s that the particle and part of the target material is vaporized and partially ionized. As the ionized cloud expands, with the more mobile electrons on the leading edge, the resulting ambipolar electric field results in a voltage pulse on a monopole electric antenna used by the RPWS. Alternately, when a dipole antenna is used, as is the case for the observations in this paper, the voltage pulse is likely related to the asymmetric collection of electrons by the two antenna elements as described by Gurnett et al. (1983) or an asymmetric ambipolar electric field. Fig. 1 shows a waveform sample showing the impulsive signature of several impacts using the dipole antenna configuration. It is clear from Fig. 1 that such waveforms provide an excellent means by which to count impacts, leading to the fluxes and, hence, number densities of the grains above a given mass threshold. We use these waveform measurements to study the flux and mass of particles in the E ring, particularly near the orbit of Enceladus.

Dust measurements with the RPWS are complementary to those made by the dedicated dust instrument on Cassini, the CDA (Srama et al., 2004). Since, in principle, the entire spacecraft is a target for dust impacts, the RPWS has a much larger collecting area than CDA and, probably more importantly, the RPWS is, to first order, not reliant on a specific spacecraft attitude to detect dust. Hence, it is possible for RPWS to detect dust more or less continuously through the orbit, whereas CDA requires favorable spacecraft attitudes to perform its measurements. On the other hand, CDA is designed to measure both the velocity and mass of dust grains and can do elemental analyses of

them. RPWS can estimate the mass of impacting particles, but has no way to distinguish between a small, fast grain and a slower, larger one, both of which could produce identical signatures in the RPWS data. Although in some cases, it is reasonable to assume an orbit, e.g. circular, low inclination orbits, in order to estimate the velocity. Finally, the minimum detectable mass of the RPWS, while dependent on several parameters, is larger than for CDA. In this paper, with relative impact speeds of order 8 km/s, the RPWS is thought to be sensitive to water ice grains of radius ~ 2.4–$3.3\,\mu m$ and larger. Initial reports of dust impacts observed by the RPWS between the F and G rings before and after the Cassini orbit insertion at Saturn are given by Gurnett et al. (2005) and Wang et al. (2006).

This work utilizes wideband waveforms collected with the 10-kHz wideband receiver of the Cassini RPWS using the *x-axis* dipole antenna as input. The waveforms consist of a variable number of samples, typically of order 2000, comprising 8-bit samples of the voltage at the electric preamplifier input at a sampling rate of 27.777 kHz. A detailed description of the RPWS is given by Gurnett et al. (2004).

2. Equatorial radial scans

Most of the observations presented here are derived from waveforms similar to those in Fig. 1 that are telemetered to the ground and analyzed there. There is a rudimentary on-board dust detection algorithm running in the RPWS that counts events that meet a rather stringent criterion for dust impacts that is basically a minimum slope in the impulse waveform. However, the onboard algorithm has some known deficiencies and simplifications that are driven by limited code space and computation resources. We have been able to replicate the output of the on-board algorithm using waveforms that have been transmitted to the ground in order to understand the output of the algorithm. In short, we believe the on-board algorithm generally has a much higher effective threshold than that which can be applied to waveforms on the ground, such that the size threshold for the algorithm is likely several microns. Furthermore, this simple algorithm has an effective mass threshold that varies with the gain of the receiver. Nevertheless, the onboard algorithm provides unique relative impact rate data. These data are used in Figs. 2 and 3 to show near-equatorial relative impact rates inside of about 8 R_S. Both of these illustrations show peaks in the dust flux near the orbit of Enceladus, during both inbound and outbound portions of Cassini's trajectory, demonstrating the ring-like nature of this population. Note that the temporal resolution for these plots is 30 min, so the accuracy of the position of the peaks relative to 3.95 R_S is poor. Further, a spline fit is used between the points, so the slopes and variations between the 30-min rates are more due to the fit than any real variation.

While the data in Figs. 2 and 3 certainly point to local maxima at the orbit of Enceladus, the limitations in the
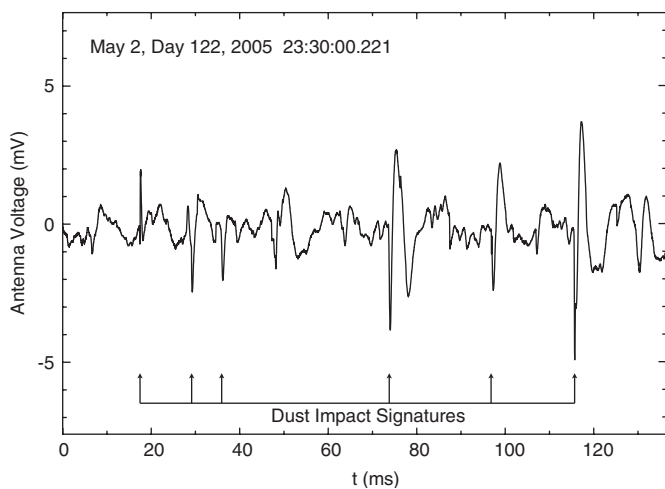

Fig. 1. Typical E ring dust impact signatures observed by the RPWS in 10-kHz wideband waveforms using the *x-axis* dipole antenna.

Orbit 3 Onboard Dust Counter Impact Rate
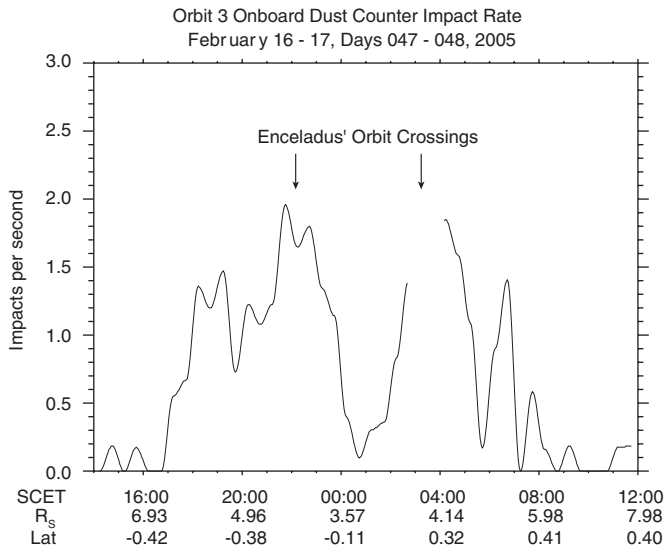February 16 - 17, Days 047 - 048, 2005

Fig. 2. An equatorial radial scan of dust impacts vs. time using an onboard algorithm for orbit showing peaks near the orbit of Enceladus. The onboard algorithm has a higher threshold for dust impacts than ground software and has some simplifications, which complicate the interpretation of these data. Nevertheless, the relative impact rates strongly suggest a durable peak near the orbit of Enceladus.

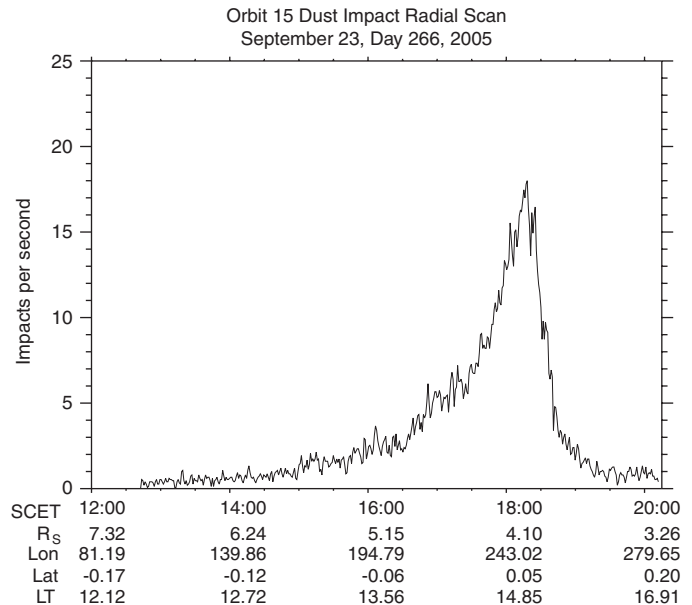Orbit 15 Dust Impact Radial Scan
September 23, Day 266, 2005

Fig. 4. A near-equatorial radial scan of dust impacts using high-resolution data telemetered to the ground crossing the orbit of Enceladus. The size threshold for detection used in this analysis is about 2.4 μm.

RPWS Orbit 4 Onboard Dust Counter Impact Rate
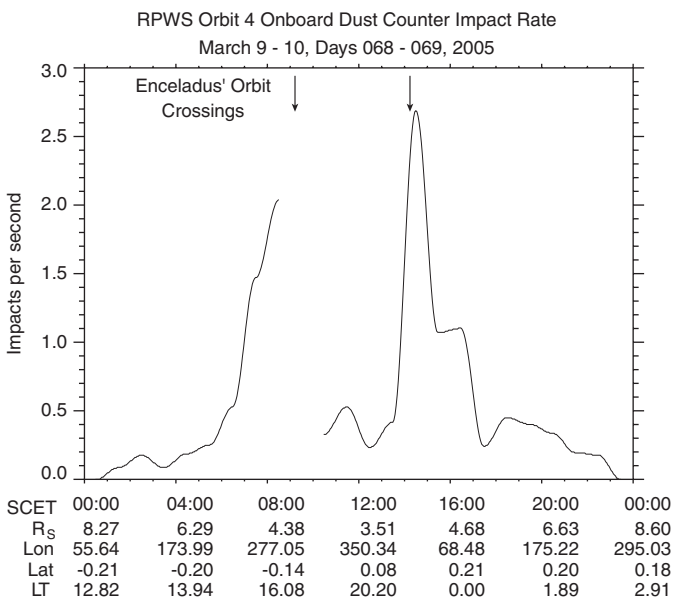March 9 - 10, Days 068 - 069, 2005

Fig. 3. A radial scan of dust impacts vs. time similar to that in Fig. 2 for orbit.

algorithm and the temporal resolution do not allow for a quantitatively accurate radial variation of dust flux in this region. Fortunately, a long series of waveform data was obtained from the inbound, nearly equatorial, crossing of Enceladus' orbit during orbit 15. An algorithm is used which has its roots in the one used by Gurnett et al. (1983) to count dust impacts recorded in the Voyager plasma wave instrument wideband data. The current algorithm uses a slope criterion that searches for an impulse whose

leading edge exceeds a jump of 0.5 mV within 108 μs and also performs a cross-correlation with a model dust impact waveform, which ensures that a characteristic recovery signature is present. For the present work, a crosscorrelation value exceeding 0.5 is required. The cross-correlation test is required to eliminate certain high frequency waves and electrostatic structures which otherwise might satisfy the slope criterion. The wideband waveforms are very data volume intensive; even with lossless compression, nearly 28 thousand 8-bit samples per second is a large data rate. Hence, a ~2000-point waveform series is collected periodically, typically once every $n = 125$ ms. If $n = 1$, the duty cycle is approximately 60%. For values of $n > 1$, the duty cycle is proportionately lower. As can be seen in Fig. 1, an individual dust impact, including the recovery time, is typically of the order of a few ms, so there is ample opportunity to find dust impacts within the ~2000-sample waveforms. Since nearly simultaneous impacts are excluded, that is, impacts that occur within a millisecond of a previous impact, the duty cycle is also decreased by a deadtime of 1 ms. For the data presented herein, impact counts are collected over 1-min intervals to improve the counting statistics. The counts are converted into impact rates by accounting for the duty cycle, so that the rates reported are those that would be measured if the sampling were continuous. Specifically, the rate is determined by dividing the number of impacts detected during a continuous series of waveforms by the duration of the series less 1 ms deadtime for each impact.

Fig. 4 shows the count rates, with 1-min resolution, for the trajectory from about 7 to 3 R_S showing a very sharp peak at about 4 R_S. Note that the rates here are more than an order of magnitude greater than those given in Figs. 2
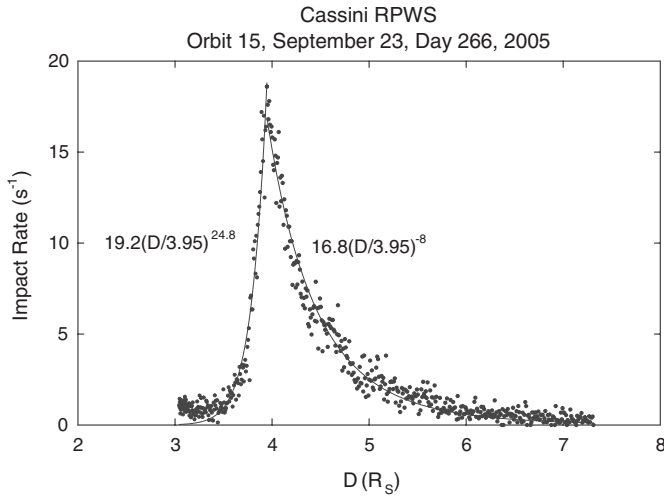
Fig. 5. Power-law fits to the radial scan shown in Fig. 4. The power law in radial distance relative to the position of the orbit of Enceladus is suggested by Showalter et al. (1991).

and 3 because the ground analysis allows a smaller mass threshold. Hence, given a power law size distribution of masses as we demonstrate below, the onboard algorithm will detect considerably fewer particles. The character of the rate plot in Fig. 4 is very reminiscent of the empirical model used by Showalter et al. (1991) employing two different power law fits inside and outside of the orbit of Enceladus. Hence, in Fig. 5 we show fits to functions of the form $\alpha(\rho/3.95)^\gamma$ for the data inside and outside 3.95 R_S where ρ is the distance in R_S from Saturn's rotational axis. The fit parameter α is related to the peak impact rate at 3.95 R_S. We choose 3.95 for the breakpoint not only because it is a reasonable match to the peak in the radial distribution curve, but also because Showalter et al., indicate that the peak in the optical data are at a distance which is indistinguishable from the orbit of Enceladus. The fits we obtain appear to be remarkably good, except for the asymptotic value inside of 3.95 where there are residual rates in excess of the model. The power law fits have exponents of $\gamma_i = 24.8$ inside of the orbit of Enceladus and $\gamma_o = -8$ outside. Showalter et al. (1991) had $\gamma_i = 15$ and $\gamma_o = -7$ from optical remote sensing measurements equivalent to the column integrated radial profile of the E ring. While the fits presented in Fig. 5 are quantitatively different from those given by Showalter et al. (1991), certainly they are qualitatively similar, in the sense that the distribution of dust outside 3.95 R_S falls off much more slowly than the inner distribution. These data strongly support the idea of a source of dust at Enceladus with a very narrow concentration at its orbit. Further, the variation in rate as a function of radial distance can be explained, in large part, by eccentricities in the dust particle orbits. Nevertheless, the residual impact rates inside 3.95 R_S also suggest that there may be a source of dust inside the orbit of Enceladus.

3. Vertical structure of the E ring near the orbit of Enceladus

In this section we discuss the vertical structure of the E ring using crossings of the ring near Enceladus' orbit on trajectories with non-zero inclinations. Fig. 6 shows impact rate versus z, the distance from the equatorial plane, using 10-kHz waveforms from orbit 7 that are telemetered to the ground like those shown in Fig. 1. The equator crossing occurred at a distance of 3.91 R_S from Saturn, very close to the orbit of Enceladus at 3.95 R_S. We assume that the form of the variation in dust flux with z can be modeled using a Gaussian distribution. However, the above discussion demonstrates that there are strong radial gradients in the dust flux both inside and outside of the orbit of Enceladus, hence, it is necessary to include this in the model since Cassini moves approximately 0.1 R_S during the time of interest. Therefore we model the rates in Fig. 6 with the following:

$$R = R_0 + R_1 f(\rho) \exp\left[\frac{-(z - h)^2}{L^2}\right], \qquad (1)$$

where R is the total rate, R_0 is a constant background rate, z is the distance from the equatorial, plane, h is a vertical offset, and L is effectively a 'scale height' describing the extent of the vertical distribution. The function $f(\rho) = (\rho/3.95)^\gamma$, where ρ is the distance from Saturn's rotational axis and $\gamma_i = 24.8$ and $\gamma_o = -8$ inside and outside of 3.95 R_S, respectively, as determined above. Gurnett et al. (1983) found a disk plus halo type of distribution modeled by a double Gaussian fit was applicable for the vertical distribution near the G ring and Wang et al. (2006) found a good fit for the vertical distribution between the F and G rings with a double Gaussian. A double Gaussian fit was
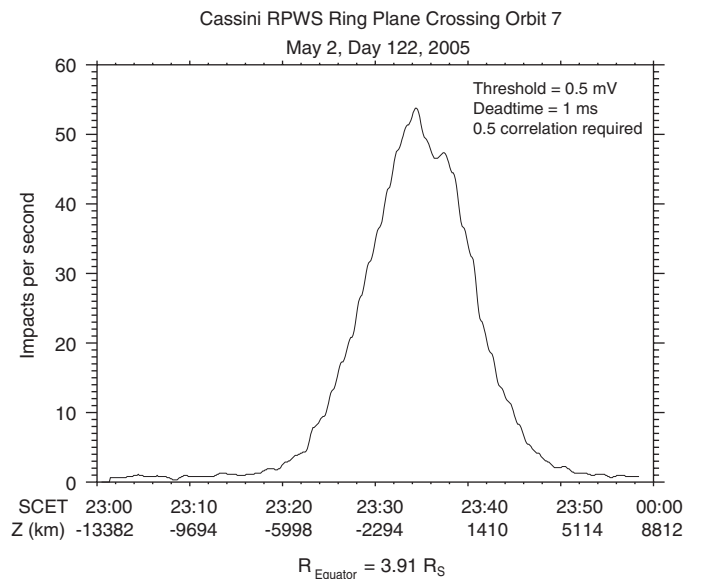

Fig. 6. Impact rate vs. time for the orbit 7 ring plane crossing. Cassini's trajectory is inclined with respect to the equator with the equator crossing occurring just inside the orbit of Enceladus at 3.91 R_S.

also attempted for this and other E ring vertical distributions, but the number of particles in the second Gaussian term was very small, of order 1, or less, so we conclude that unlike the situation closer to the main ring system, there seems to be no disk plus halo distribution of dust in the E ring near the orbit of Enceladus. The scale height is found to be 2813 km and there is an offset of about 200 km below the geometric equator. The fit is plotted along with the orbit 7 observed count rates in Fig. 7.

We note that there is evidence for some structure near the peak counting rates in Fig. 7 that is not well modeled by the Gaussian fit. While these variations are of the order of the error statistics ($R^{1/2}$), they appear in each of the inclined crossings. Recent edge-on images of the E ring by Cassini appear to show structure at about the same vertical scale, so these variations may be more than statistical (J. Burns, personal communication, 2005).

With peak impact rates R of about $50\,s^{-1}$ for the orbit 7 equator crossing, it is straightforward to determine the number density n of dust at or above the mass threshold for the RPWS measurements from $n = R/Av$, where A is the cross-sectional area of the spacecraft and v is the relative impact speed. In general, it is difficult to know the proper area to use since the yield factor, K, of the impacts is a function of target material. But, for simplicity, we take the area of the 4-m high gain antenna, $12.6\,m^2$ as an approximation for A even though the impact direction for most of the E ring crossings are at rather large angles from the high gain antenna axis. For this time period, the relative speed with respect to circular Keplerian orbits is about 8 km/s. Hence, we obtain $n \sim 5 \times 10^{-4}\,m^{-3}$. This is equivalent to one particle in a cube $\sim 12.5\,m$ on a side. It is important to realize that this is the density of particles at and above the mass threshold of the RPWS. Appendix A addresses initial attempts at reconciling the impact rates reported here and those observed by the high rate detector (HRD) portion of the CDA instrument.

A number of inclined E ring crossings have been completed, similar to that described from orbit 7. These demonstrate similar variations in impact rates as a function of z about the equator. The peak impact rate, the fit parameter R_1, the scale height L, vertical offset of the distribution, difference in longitude of Cassini relative to Enceladus at the time of the crossing $\Delta\lambda$, and the distance of the impact rate peak from the rotation axis ρ, are all given in Table 1. The peak rates vary by about a factor of 2 from one crossing to the next and do not seem to show any clear variation with radial distance from Saturn. The parameter R_1 is the peak of the E ring at $3.95\,R_S$ at the equator. The largest rates are at $\Delta\lambda \approx 60°$ and $\approx 119°$ leading Enceladus in its orbit, perhaps consistent with concentrations at the L4 Lagrangian point. However, there are too few points determined, here, to be conclusive on this issue. And, there are no measurements, yet, near the L5 point trailing Enceladus. Note that the scale height L is determined here only in a very narrow radial distance range between 3.91 and $3.96\,R_S$. We have made no attempt, yet, to determine L at other distances, hence, we make no claim as to the variation of L, or lack thereof, with radial distance.

4. Mass estimates

In principle, the mass of the impacting particles can be derived from the impact signatures, since the magnitude of the voltage pulse is proportional to the mass of the impacting particle. However, the voltage pulse is also a function of the velocity of the impact, which is not independently measured by the RPWS, so it is simply assumed that the velocity of the particle is the vector

Cassini RPWS Model Fit to Impact Rate
Orbit 7, May 2, Day 122, 2005

$R_0 = 1.4$ impacts/sec
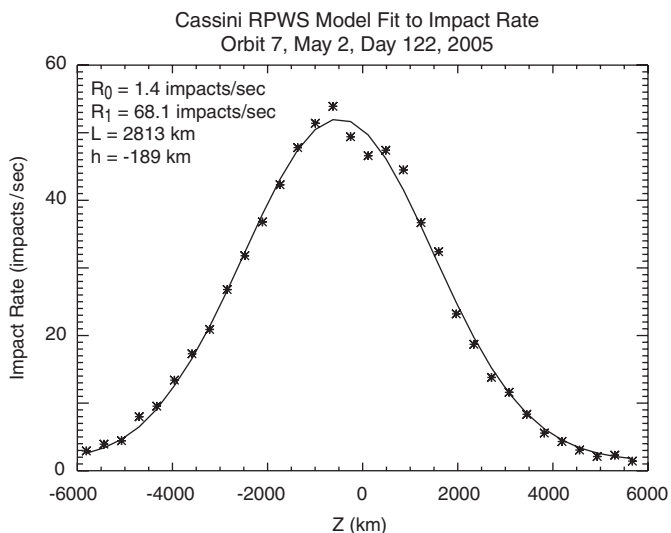$R_1 = 68.1$ impacts/sec
$L = 2813$ km
$h = -189$ km

Fig. 7. A model fit to the impact rate data shown in Fig. 6 as a function of the height above the equator. The model incorporates the power law radial model shown in Fig. 5 and a Gaussian in z, the distance from the equatorial plane.

Table 1
Characteristics of the vertical distribution of dust in the E ring near Enceladus' orbit

Orbit	Date	Time	Rate (s^{-1})	R_1 (s^{-1})	L (km)	h (km)	$\Delta\lambda$ (°)	ρ (R_S)
7	May 2, 2005	23:34:51	52	68	2813	−189	60.1	3.910
9	June 8, 2005	08:26:39	26	30	2450	563	−134.2	3.913
10	June 26, 2005	13:28:52	41	44	3130	28	−239.7	3.936
12	August 2, 2005	03:31:47	28	28	3401	−199	228.1	3.956
13	August 20, 2005	08:59:24	49	55	3240	8	118.7	3.942

Table 2
Masses, sizes, and mass distributions determined for several E ring crossings

Orbit	Date	Time	α	m_{rms} (g)	r (μm)
7	May 2, 2005	23:34:51	3.38	3.4×10^{-10}	4.5
9	June 8, 2005	08:26:39	2.61	1.9×10^{-10}	3.7
10	June 26 2005	13:28:52	2.49	2.3×10^{-10}	3.9
12	August 2, 2005	03:31:47	2.55	1.5×10^{-10}	3.4
13	August 20, 2005	08:59:24	2.90	2.8×10^{-10}	4.2
15	September 23, 2005	16:00–19:00	2.86	1.5×10^{-10}	3.4

difference of the spacecraft velocity and a particle in a prograde circular Keplerian orbit. It is also likely that the pulse height is dependent on the target material and perhaps even the location of the impact on the spacecraft relative to the RPWS antennas. Finally, most of the observations in this paper are acquired using the *x-axis* dipole antenna. As pointed out by Gurnett et al. (1983), using the dipole configuration introduces a coupling coefficient into the pulse height analysis that is related to how much of the charge yield is collected by the antennas, hence, can only be estimated. Hence, mass estimates derived from the pulse height have large uncertainties. Another method, used by Aubier et al. (1983) to analyze Voyager 2 planetary radio astronomy observations in Saturn's ring plane, uses the voltage spectrum of impacts with a monopole antenna to determine the root mean square mass of the impacting dust particles. Wang et al. (2006) have adapted this technique to the study of dust impacts observed by the Cassini RPWS between the F and G rings around the time of Saturn orbit insertion (SOI) on July 1, 2004. During those ring plane crossings, the impact rates were of order $1000 \, s^{-1}$, and the expected f^{-4} spectrum and its breakpoint were clearly visible in spectra acquired with the *w-axis* monopole antenna. Since the rate of impacts in the E ring is substantially smaller, this technique cannot be directly applied. Furthermore, during the SOI time period, waveforms were also acquired, simultaneously, using the *x-axis* dipole antenna. Hence, we can use the mass determination near SOI from Wang et al. (2006) and scale the E ring measurements using the dipole waveforms, acquired in the same way as near SOI.

The basis for the scaling is:

$$V = Kmv^{\beta}, \tag{2}$$

where V is the voltage produced by the impacts, K is the yield constant, m is the particle mass, v is the relative speed of the impact and β is an empirically-determined constant. We assume that K is the same for both SOI and E ring impacts. Adams and Smith (1971) determined a value of 3.2 for β. Using the method of Aubier et al. (1983), Wang et al. (2006) have found the root mean square value near SOI for m_{SOI} to be 7.7×10^{-11} g. From the dipole waveform measurements they have also determined the root mean square value of V_{SOI} to be 6.65 mV. Hence, we can

then use the ratio

$$\frac{V_{SOI}}{V_{E \, ring}} = \frac{m_{SOI}}{m_{E \, ring}} \left(\frac{v_{SOI}}{v_{E \, ring}} \right)^{\beta}, \tag{3}$$

where $v_{SOI} \approx 16 \, km/s$ and $v_{E \, ring} \approx 8 \, km/s$ are the relative speeds of the impacts near SOI and in the E ring, respectively, to determine $m_{E \, ring}$ or, using

$$m = \tfrac{4}{3}\pi r^3 \rho_m \tag{4}$$

and $\beta = 3.2$, the radii of the SOI and E ring particles scale as

$$\frac{V_{SOI}}{V_{E \, ring}} = 9.2 \left(\frac{r_{SOI}}{r_{E \, ring}} \right)^3. \tag{5}$$

The root mean square voltage for impacts during the orbit 7 E ring crossing was 3.23 mV, hence, the root mean square mass of the orbit 7 grains is 3.4×10^{-10} g and the corresponding radius, using $\rho_m = 0.92 \, g \, cm^{-3}$, is 4.5 μm. The root mean square mass and radius for other E ring crossings are given in Table 2. All of these crossings have root mean square radii near 4 μm, but as noted below, the RPWS threshold for detection is about 2.4 μm or larger. It should also be noted that Wang et al. (2006) caution that because the value of the yield must be estimated, there is a possibility of a 'significant' uncertainty in their mass determination, which would also be applicable to this study.

Fig. 8 is a voltage distribution for the orbit 7 impacts showing the fraction of dust impacts in successive 0.5 mV ranges. However, since V is proportional to m, the plot is also a mass distribution. Using Eq. (3), we can add the mass scale to the top of Fig. 8. Based on the mass scaling used for Fig. 8, it is clear that the 0.5 mV threshold corresponds to about 2.4 μm particles. (But, see the discussion in Appendix A about possible errors in the estimate of the mass threshold, which could adjust this upwards to about 3.3 μm.) Above about 4 μm, the size distribution is well characterized by a power law of the form $m^{-\alpha}$ with $\alpha = 3.38$. This is very similar to the $m^{-3.1}$ power law used to model ejecta from Enceladus (and the other icy moons) by Juhász and Horányi (2002). Below $\sim 4 \, \mu$m, the distribution rolls off, deviating from the power law.

Similar mass distributions were calculated for the other ring plane crossings near the orbit of Enceladus listed in Table 2 and the value of the power law exponent α is listed for each as well as the root mean mass and radius for each crossing. Furthermore, we calculated a mass distribution for the radial profile from orbit 15. This distribution was characterized by $\alpha = 2.86$. The latter distribution is shown in Fig. 9. In this distribution, there appears to be a sharp cutoff near 7 mV or about 6 μm beyond which no particles are found. Further, other than the smallest voltage step (mass bin) the distribution is quite linear in this log–log presentation. In fact, this distribution is more similar to those of the distributions of orbits 9, 10, 12 and 13 than is that in Fig. 8 from orbit 7. While it would be simple to call the orbit 7 distribution 'different', it does have the largest population of impacts of the set. If we simply average the exponents for each of the distributions in Table 1 plus that of the orbit 15 radial scan, we obtain ave $\alpha_{ave} = 2.80 \pm 0.33$. Hence, even though it is apparently different from the other distributions, its exponent is less than two standard deviations from the mean.

It is commonly reported that the 'typical' particle size in the E ring, however, is very close to 1 μm, below the size threshold based on 0.5 mV threshold used here. An $m^{-2.80}$ power law is not inconsistent with a peak near 1 μm. And, the apparent cutoff near ~6 μm observed in most of the distributions is also consistent with a narrow distribution often mentioned for E ring particles. The rolloff in the lowest mass bin in Fig. 9 and more severely in a broader range of masses in Fig. 8 is not well understood at this point. However, it is possible that if there is some variation in pulse height with target material or geometry for an impactor with a given mass, then some of the particles ostensibly within the lowest mass bins may not be detectable and, therefore, these smallest particles may be under counted.

5. Discussion and conclusions

We have shown measurements of a localized population of few-micron-sized dust particles near the orbit of Enceladus. This peak in the E ring is well known from optical measurements and is the basis for suggestions that Enceladus is the primary source of the E ring (Haff et al., 1983). The peak densities observed for particles above the RPWS detection threshold are in the range of 5×10^{-4} m^{-3}. Following the simple empirical form of the E ring model used by Showalter et al.(1991), the flux of dust varies radially inside of 3.95 R$_S$ as $(\rho/3.95)^{24.8}$ and outside of this radius as $(\rho/3.95)^{-8}$. The vertical structure of the E ring near the orbit of Enceladus is well modeled by a Gaussian distribution with a scale height of about 2800 km. There is a vertical offset of the peak flux from the geometric equator by up to a few 100 km. The peak in the ring density varies by about a factor of two from one crossing to another. There are too few points to draw a sound conclusion, but the maximum densities currently in

hand are found in the vicinity of the L4 Lagrangian point. The size threshold for the measurements presented is about 2.4 μm (or perhaps as high as 3.3, according to the discussion in Appendix A), somewhat above the expected peak in the E ring size distribution at about 1 μm. Above this threshold, the root-mean-square radius determined for these particles is about 4 μm, assuming water ice. The particle mass distributions measured are proportional to $m^{-2.80}$.

In spite of the fact that the size threshold for the RPWS measurements presented here misses the bulk of the 1 μm population thought to dominate the E ring (Showalter et al., 1991; Hamilton and Burns, 1994), these observations appear to fit quite well with previous work, but have the advantage of in situ evidence for inferences based, in many cases, on remote optical measurements, sometimes limited in resolution. The preponderance of previous observations and dynamical work suggests the E ring comprises a narrow distribution of particles near 1 μm. Dynamical considerations (cf. Burns et al., 1984; Hamilton and Burns, 1994) suggest that 1 μm particles are favored because the net effect of gravitational forces, the Lorentz force, and radiation pressure lead to elliptical orbits which ensure energetic collisions with, primarily, Enceladus to continually replenish the ring. The present observations suggest that the larger particles observed by the RPWS are simply the large-radius tail of this distribution. That the particles detected by RPWS show a qualitatively similar radial variation to the empirical model given by Showalter et al. (1991) lends credence to the notion that these larger particles are apparently just the higher mass portion of the E ring distribution. On the other hand, Showalter et al. (1991) claim that no power-law size distribution is compatible with the photometry measurements. The resolution of this possibly lies in a more detailed accounting of the photometric response to a more complicated particle size distribution. It will be interesting to see whether CDA size distributions extending to smaller sizes will clarify whether RPWS is observing an additional component to a narrow distribution about 1 μm or if it is just a high mass tail to the main 1-μm distribution.

The equatorial radial profile modeled in Fig. 5 is of the same form as the empirical model by Showalter et al. (1991) but has significantly different power law dependencies, especially on the inside portion of the profile. However, it seems likely that the available spatial resolution would yield somewhat weaker gradients than the present measurements. For example the Keck point spread function is about 7000 km (personal communication, I. dePater, 2005) or about 0.2 R$_S$. The measured dust flux drops by a factor of 2 in just 0.1 R$_S$ inside of the orbit of Enceladus. So it is not surprising that the stronger gradient resolved by the Cassini in situ measurements would be unresolved by a ground-based observation such as those analyzed in the Showalter et al., paper.

From Fig. 7, one can determine the full-width at half-maximum (FWHM) of the E ring, which is about 4700 km.

This can be compared to a Hubble determination of about 8000 km for the FWHM thickness of the ring near the orbit of Enceladus (Sicardy et al., 1996). Here, we cannot argue a lack of resolution for the difference, since the Hubble resolution is about 700 km, according to Sicardy et al. Furthermore, an examination of other values of L in Table 1 suggests that other measurements of the FWHM by Cassini do not yield a value as large as the Hubble value, hence, the difference does not appear to be a longitudinal variation. We suggest, however, that since RPWS does not measure the 1 μm particles that make up the bulk of the particles in the E ring, it is possible that these smaller particles are less confined to the equator and that optical observations may see a thicker ring due to these smaller particles. This difference in 'scale height' for different sized particles is actually observed between the F and G rings, for example (Wang et al., 2006). Interestingly, though, some of the 'notch' models for the E ring thickness in Showalter et al. (1991) appear to be in the range of the 4700 km reported here.

As discussed in detail in Appendix A, the determination of mass of dust particles from the RPWS is still uncertain. Also, at face value, the dust flux measured by the CDA/HRD instrument is significantly greater than that measured by RPWS. The Appendix suggests that this difference can be explained by some combination of a smaller effective collecting area than that assumed for RPWS or a larger mass threshold for the RPWS than that determined by scaling from the Wang et al. (2006) results. But, a straightforward correction of the RPWS mass threshold to 1.4×10^{-10} g or 3.3 μm for the E ring measurements given here brings the two data sets into reasonable agreement. In any case, the size distributions and the models for the radial and vertical profiles are not affected by these uncertainties in the absolute mass determination.

Finally, we mention the recent observations by the CDA/HRD (Spahn et al., 2006) within the Hill sphere of Enceladus which appear to be consistent with a global source of sputtered particles but with a dominant source of particles emanating from the southern hemisphere where evidence for recent geologic activity and local hot spots have been reported. The size threshold of the HRD is similar to the threshold used in this paper. Hence, the narrow peak of the E ring at Enceladus is strongly tied to a fresh source of material coming from the moon.

Acknowledgments

Appendix A

For several of the E ring crossings discussed in this paper the CDA's HRD was operational and counting dust impacts. The HRD uses a collecting area of 50 cm^2 (Srama et al., 2004) and is sensitive to ice particles of radius 2 μm or larger at the relative velocities of impacts experienced in the E ring. It is reasonable, then, to ask if the impact rates observed by the RPWS are consistent with the rates observed by the HRD. For example, for the June 8, 2005 crossing, RPWS measured a peak impact rate of 26 s^{-1}. As mentioned in this paper, one can approximate the cross-sectional area of the spacecraft by the area of the high gain antenna, or 12.6 m^2. Hence, the particle flux is 2.1 m^{-2} s^{-1}. For this same crossing, the HRD detected impacts at the rate of 0.31 s^{-1} (S. Kempf, personal communication, 2006) using a well-defined collecting area of 50 cm^2. Hence, the flux given by the HRD is 62 m^{-2} s^{-1}, a factor of about 30 larger than the RPWS flux. Here, we attempt to understand the nature of this apparent mismatch.

One uncertainty in the RPWS observations is the effective collecting area. A simple approximation to this is the actual cross-sectional area of the spacecraft subtended perpendicular to the direction of relative dust velocity. Cassini is a complex body including a number of booms and appendages. One simplification might be to use the area of the 4-m diameter high gain antenna, which is 12.6 m^2. However, as pointed out by Gurnett et al. (1983), the charge yield of an impact is a strong function of target material. On Voyager, it was thought that the gold plated record cover had the highest yield and materials like thermal blankets had poor yields. Hence, one can write down an effective area, which is a sum of the various target material areas weighted by their effectiveness in producing charge $A_{eff} = A_1\varepsilon_1 + A_2\varepsilon_2 + A_3\varepsilon_3 + \ldots$, the epsilons (efficiencies) are normalized to lie in the range of 0 to 1. Gurnett et al. (1983) used an effective area of 1.66 m^2 for the Voyager 2 spacecraft, but there was no means with which to verify this value.

On Cassini, the HRD provides an independent measure of the dust flux, since it has a well defined collecting area and a calibrated mass threshold (albeit using iron impactors in the mass range of interest). Table A1 provides the peak impact rates for both the RPWS and the HRD (S. Kempf, personal communication, 2006) using the 2 μm threshold, for the moment assumed to have similar mass sensitivity to the RPWS.

With the simple assumptions above we can write

$$\frac{R_{HRD}}{A_{HRD}} = \frac{R_{RPWS}}{A_{eff}}, \tag{A.1}$$

Table A1
A comparison of peak impact rates observed by RPWS and the CDA/HRD

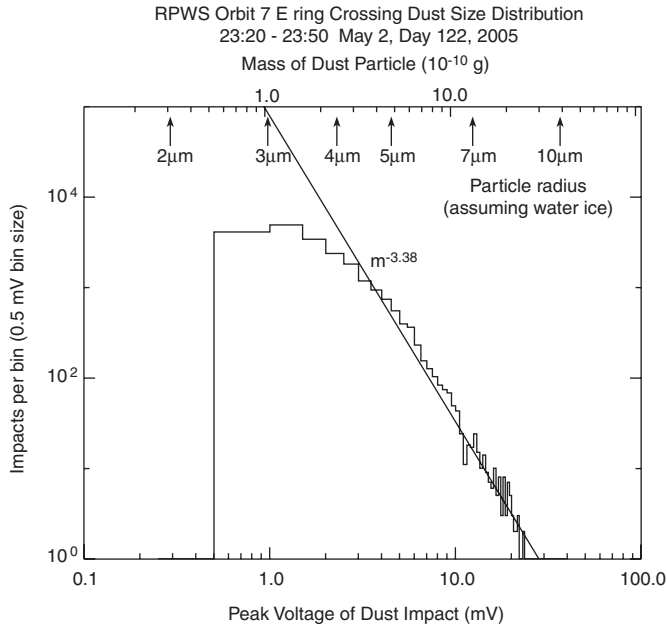| Date	Peak R_{RPWS} (s^{-1})	Peak R_{HRD} (s^{-1})	A_{eff} (m^2)
May 2, 2005	52	0.56	0.46
June 8, 2005	26	0.31	0.42
June 26, 2005	41	0.78	0.26
August 20, 2005	49	0.62	0.40

Fig. 8. A plot of the distribution of peak voltages of impacts during the orbit 7 crossing. Since V is proportional to mass, this is also a mass distribution. The mass scale is set by comparing the relationship between the root mean square voltage to the root mean square mass determined by scaling from Wang et al. (2006) for equator crossings between the F and G rings where the mass can be more reliably determined using the technique of Aubier et al. (1983). The distribution varies as $m^{-3.38}$ above about 4 μm, but rolls over for smaller particles.

where R_{PWS} and R_{HRD} are the peak impact rates recorded by the RPWS and HRD, respectively, A_{HRD} is the collecting area of the HRD, or $50\,\mathrm{cm}^2$, and A_{eff} is the effective collecting area of the RPWS.

The last column in Table A1 gives A_{eff} calculated from Eq. (A.1) for each of the E ring crossings for which we have peak impact rates for both instruments. The average A is $0.39\,\mathrm{m}^2$, but the value for Jun. 26 is somewhat of an outlier.

However, as shown in Figs. 8 and 9, the size threshold of the RPWS for the ~8 km/s impact speeds in the E ring and the 0.5 mV voltage threshold used for this study is not 2 μm, but closer to 2.4 μm, or about 5×10^{-11} g. Further, it is clear that all of the size distributions examined in the E ring using the RPWS data including those shown in Figs. 8 and 9, show a rolloff in the size distribution below 3 to 4 μm. Given extensive evidence in the literature that the E ring is composed of predominantly 1 micron-sized particles, it seems unlikely the true size distribution exhibits such a rolloff. In fact, the magnitude of a dust impact signature observed with the dipole antenna is likely a function of the position of the impact. This can be viewed as a distribution of impact magnitudes about a nominal value. Hence, poorly placed impacts of near-threshold dust grains may not actually be detected.

The RPWS threshold, then, cannot be taken to be equal to 2 μm and directly compared to the HRD rate. However, we can estimate the number of impacts the RPWS would see if it had a 2 μm size threshold by integrating under the power law curves determined for each crossing similar to
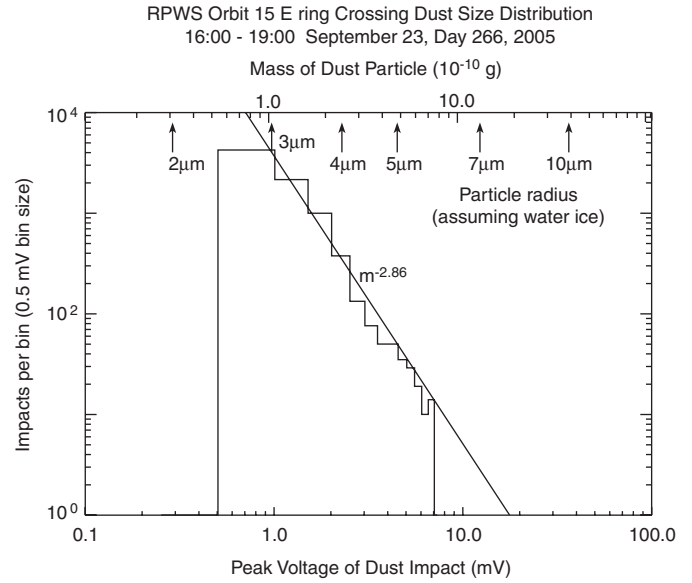

Fig. 9. A mass distribution, similar to that in Fig. 8, but for the orbit 15 radial scan observations in Fig. 4. In this case, the power law exponent is −2.86. Note that the rolloff in count rates shown in Fig. 8 is only present in this example for the lowest voltage (mass) bin and that there is a high-mass cutoff in the distribution not apparent in Fig. 8.

those illustrated in Figs. 8 and 9, down to the $\sim 3 \times 10^{-11}$ g corresponding to 2 μm water ice grains using

$$N_{est} = \int_{V_{MIN}}^{V_{MAX}} C V^{-\alpha}\, \mathrm{d}V, \qquad (A.2)$$

where N_{est} is the estimated number of impacts, C is a constant, V is the impact voltage, and α is the exponent given in Table 2. Since the particle mass is proportional to V, we integrate over impact voltage. Extrapolating the results from Wang et al., (2006) V_{MIN} is set to 0.3 mV, corresponding to the voltage 2 μm particles would have. The upper limit V_{MAX}, corresponds to the largest grains detected, typically about 10^{-9} g.

By dividing this integrated impact count by the observed impact count, a multiplicative factor can be determined. The observed impact rates can be multiplied by this factor in order to estimate the number of grains of radius 2 μm and larger which would be detected if the RPWS threshold were the same as HRD and there was no variation in impact amplitude with impact location. This corrected rate can then be compared to the HRD rate using Eq. (A.1) to derive an adjusted effective area.

Table A2 gives N_{est} the integrated impact count using the measured size distribution extrapolated down to 3×10^{-11} g, the observed impact count N_{obs}, the peak impact rate R_{RPWS}, the resulting corrected rate R^*, and finally, the effective area using the corrected peak impact rate A_{eff}^*. The results of this, however, are unsatisfactory because of the large variation in the effective area, ranging from $1.31\,\mathrm{m}^2$ for the June 26 crossing to $\sim 24\,\mathrm{m}^2$ for the May 2 crossing. The latter is somewhat larger than the spacecraft, hence is questionable. The May 2 distribution,

Table A2
Estimates of the RPWS effective area based on integrating the size distribution to 2 μm

Date	N_{est}	N_{obs}	Peak R_{RPWS} (s^{-1})	R^* (s^{-1})	A^*_{eff} (m^2)
May 2, 2005	1,141,787	21,861	52	2716	24.3
June 8, 2005	22,272	5209	26	111	1.79
June 26, 2005	92,635	18,646	41	204	1.31
August 20, 2005	47,160	5418	49	427	3.44

shown in Fig. 8 has already been noted as being different for the strong rolloff at the smaller grain sizes. This rolloff is much more noticeable than for the other crossings. Also, the distribution is much steeper than the other distributions. These two factors lead to a very large estimate for the number of undetected small particles.

The steep mass dependence makes it difficult to accurately extrapolate the RPWS size distribution down to the stated HRD threshold, plus, the HRD threshold may be somewhat uncertain for ice grains given iron projectiles were used for the calibration of masses in the range of 10^{-10} g and less. In fact, if there is an underestimate of the mass of particles detected by the RPWS, then it might be possible to explain the mismatch in counting rates almost entirely by this error, alone, keeping the physical cross-section of the spacecraft as a collecting area. We investigate this approach, briefly.

The integral used to determine N_{est} in Eq. (2) uses the relationship between the impact voltage on the dipole antenna and the particle mass as described in the section on Mass Estimates. Since this estimate is scaled from the Wang et al. (2006) mass determination using the Aubier et al. (1983) technique and Wang et al., suggest that 'substantial' uncertainties may be involved in this determination due to the poorly know yield factor on the high gain antenna, certainly the mass estimates in this paper are at least equally subject to errors. Using the June 8, 2005 crossing as an example, we investigate how an adjustment in the relationship between impact voltage and mass might affect the counting rates. We illustrate the size distribution of this crossing in Fig. A1. Using Table A2, we can say that if we set $A_{eff} = 12.6$ m^2, that is, the area of the high gain antenna, then we can calculate that N_{est} would have to be larger by a factor of 12.6/1.79 or $N_{est} = 156,775$ in order to be consistent with the HRD rate. We vary the V_{MIN} in Eq. (2) until we obtain this value for N_{est}. The result is that instead of $V_{MIN} = 0.3$ mV, we need to use $V_{MIN} = 0.09$ mV. This amounts to saying that the mass scales in Figs. 8 and 9 must be shifted to the left so that the mass threshold at 0.5 mV is now about 1.4×10^{-10} g or 3.3 μm instead of the 5×10^{-11} g or 2.4 μm scaled from the Wang et al. (2006) result. Given the uncertainties in the mass derivation, this change of a factor of 2.8 in mass is not unreasonable.

We have considered three possible contributors to the apparent mismatch in the RPWS and HRD counting rates. First, the effective collecting area of the spacecraft may be
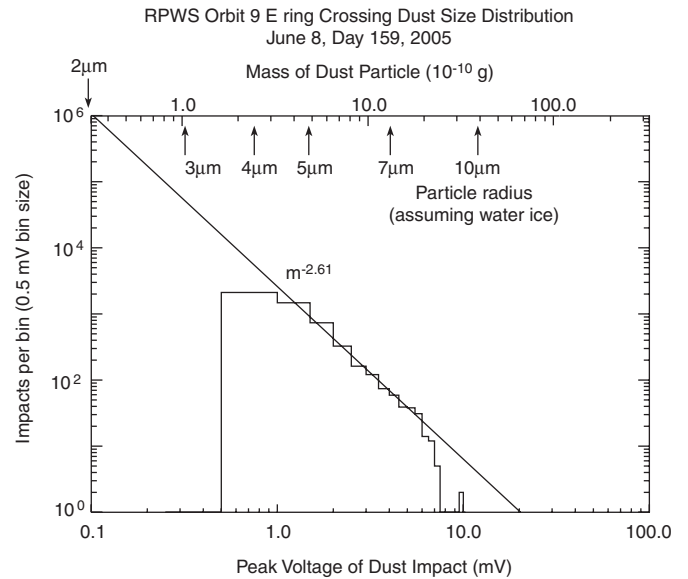

Fig. A1. A mass distribution for the E ring crossing of June 8, 2005. If the mass scale is shifted to the left (as compared to Figs. 8 and 9) the difference in dust flux observed by RPWS and the CDA/HRD can be explained entirely by a difference in mass thresholds. The mass threshold required in this case is 1.4×10^{-10} g or ice grains of radius 3.3 μm.

much smaller than the physical cross-section because of a predominance of low-yielding target materials such as thermal blankets. Second, given the mass threshold presented in this paper, the HRD detects smaller particles. Given the steep slope of the size distribution, there is a large portion of the distribution that is being counted by the HRD that are below the threshold of the RPWS. Efforts to correct for this difference in thresholds yield mixed results because of large uncertainties in extrapolating to lower mass particles. Finally, if RPWS actually has a somewhat larger mass threshold than derived from extrapolating the Wang et al. (2006) result, all of the mismatch in counting rates may be simply due to a larger difference in mass thresholds. In reality, the issue is likely a complex mix of all three of these factors. And, given the largely unknown yield as a function of target material and uncertainties in the RPWS mass threshold, it is not possible to reliably distinguish between these competing effects with the information in hand. We suggest that the simplest reconciliation of the apparent mismatch in the RPWS and HRD rates is a modest adjustment in the mass threshold of RPWS to about 1.4×10^{-10} g or 3.3 μm. Even with this uncertainty, the shapes of the RPWS impact rate profiles

and the exponent of the size distributions presented in this paper are basically unaffected.

Finally, it should be noted that this analysis takes the HRD counting rates and mass threshold provided by the CDA team at face value. We do not know what uncertainties there are in these values. As such, this appendix should be considered as only a preliminary attempt at cross calibrating the two instruments.

References

Aubier, M.G., Meyer-Vernet, N., Pedersen, B.M., 1983. Shot noise from grain and particle impacts in Saturn's ring plane. Geophys. Res. Lett. 10, 5–8.

Burns, J.A., Showalter, M.R., Morfill, G.E., 1984. The ethereal rings of Jupiter and Saturn. In: Greenberg, R.J., Brahic, A., Matthews, M.S. (Eds.), Planetary Rings. University of Arizona Press, Tucson, USA, pp. 200–272.

Feibelman, W.A., 1984. Saturn's E ring in the red spectral region. In: Brahic, A. (Ed.), Planetary Rings. CNES, Toulouse, France, pp. 99–102.

Gurnett, D.A., Grün, E., Gallagher, D., Kurth, W.S., Scarf, F.L., 1983. Micron-sized particles detected near Saturn by the Voyager plasma wave instrument. Icarus 53, 236.

Gurnett, D.A., Kurth, W.S., Scarf, F.L., Burns, J.A., Cuzzi, J.N., Grün, E., 1987. Micron-sized particle impacts detected near Uranus by the Voyager 2 plasma wave instrument. J. Geophys. Res. 92, 14,959.

Gurnett, D.A., Kurth, W.S., Granroth, L.J., Allendorf, S.C., Poynter, R.L., 1991. Micron-sized particles detected near Neptune by the Voyager 2 plasma wave instrument. J. Geophys. Res. 96, 19,177.

Gurnett, D.A., et al., 2004. The Cassini radio and plasma wave investigation. Space Sci. Rev. 114, 395–463.

Gurnett, D.A., et al., 2005. Radio and plasma wave observations at Saturn from Cassini's approach and first orbit. Science 307, 1255–1259.

Haff, P.K., Eviatar, A., Siscoe, G.L., 1983. Ring and plasma: the enigmae of Enceladus. Icarus 56, 426–438.

Hamilton, D.P., Burns, J.A., 1994. Origin of Saturn's E ring: self-sustained, naturally. Science 264, 550–553.

Humes, D.H., O'Neal, R.L., Kinard, W.H., Alvarez, J.M., 1980. Impact of Saturn ring particles on Pioneer 11. Science 207, 443–444.

Johnson, R.E., Pospieszalska, M.K., Sittler, E.C., Cheng, A.F., Lanzerotti, L.J., Sievka, E.M., 1989. The neutral cloud and heavy ion inner torus at Saturn. Icarus 77, 311–329.

Juhász, A., Horányi, M., 2002. Saturn's E ring: a dynamical approach. J. Geophys. Res. 107, 1066.

Meyer-Vernet, N., Aubier, M.G., Pedersen, B.M., 1986. Voyager 2 at Uranus: grain impacts in the ring plane. Geophys. Res. Lett. 13, 617.

Meyer-Vernet, M., Lecacheux, A., Pedersen, B.M., 1996. Constraints on Saturn's E ring from the Voyager 1 radio astronomy instrument. Icarus 123, 113–129.

Morfill, G.E., Havnes, O., Goertz, C.K., 1993. Origin and maintenance of the oxygen torus in Saturn's magnetosphere. J. Geophys. Res. 98, 11,285–11,297.

Pedersen, B.M., Meyer-Vernet, N., Aubier, M.G., Zarka, P., 1991. Dust distribution around Neptune: grain impacts near the ring plane measured by the Voyager planetary radio astronomy experiment. J. Geophys. Res. 96, 19187.

Showalter, M.R., Cuzzi, J.N., Larson, S.M., 1991. Structure and particle properties of Saturn's E ring. Icarus 94, 451–473.

Sicardy, et al., 1996. Hubble Space Telescope observations of Saturn during the August and November 1995 ring plane crossings. In: Benvenuti, P., Macchetto, F.D., Schreier, E.J. (Eds.), Science with the Hubble Space Telescope—II. Space Telescope Science Institute (STScI), Baltimore, MD, p. 546.

Spahn, F., Schmidt, J., Albers, N., Hörning, M., Makuch, M., Seiß, M., Kempf, S., Srama, R., Dikarev, V., Helfert, S., Moragas-Klostermeyer, G., Krivov, A.V., Sremčević, M., Tuzzolino, A.J., Economou, T., Grün, E., 2006. Cassini dust measurements at Enceladus and implications for the origin of the E ring. Science 311, 1416–1418.

Srama, R., et al., 2004. The Cassini cosmic dust analyzer. Space Sci. Rev. 114, 465–518.

Tsintikidis, D., Kurth, W.S., Gurnett, D.A., Barbosa, D.D., 1995. A study of dust in the vicinity of Dione using the Voyager 1 plasma wave instrument. J. Geophys. Res. 100, 1811.

Wang, Z., Gurnett, D.A., Averkamp, T.F., Persoon, A.M., Kurth, W.S., 2006. Characteristics of dust particles detected near Saturn's ring plane. Planet. Space Sci., this issue.